Geochemistry, Geophysics, Geosystems®

RESEARCH ARTICLE
10.1029/2024GC011593

Nd Isotopic Equilibration During Channelized Melt Transport Through the Lithosphere: A Feasibility Study Using Idealized Numerical Models

Mousumi Roy[1], **G. Lang Farmer**[2], **and Kellen Malone**[1]

[1]Department of Physics and Astronomy, University of New Mexico, Albuquerque, NM, USA, [2]Department of Geological Sciences and CIRES, University of Colorado Boulder, Boulder, CO, USA

Key Points:

- Trace elements in primitive basalts from southwest North America suggest both asthenosphere- and lithosphere-related signatures
- Open system interactions between ascending channelized melts and wallrock may affect the trace element composition of erupted basalts
- 1D transport models quantify the role of diffusion and wallrock assimilation to produce significant Nd isotopic shifts over 10 km of transport

Supporting Information:

Supporting Information may be found in the online version of this article.

Correspondence to:

M. Roy,
mroy@unm.edu

Citation:

Roy, M., Farmer, G. L., & Malone, K. (2024). Nd isotopic equilibration during channelized melt transport through the lithosphere: A feasibility study using idealized numerical models. *Geochemistry, Geophysics, Geosystems*, *25*, e2024GC011593. https://doi.org/10.1029/2024GC011593

Received 2 APR 2024
Accepted 11 SEP 2024

Author Contributions:

Conceptualization: Mousumi Roy, G. Lang Farmer
Formal analysis: Mousumi Roy
Funding acquisition: Mousumi Roy
Investigation: Mousumi Roy
Methodology: Mousumi Roy, G. Lang Farmer
Project administration: Mousumi Roy
Resources: Mousumi Roy
Software: Mousumi Roy, Kellen Malone
Supervision: Mousumi Roy
Validation: Mousumi Roy
Visualization: Mousumi Roy

Abstract This study is motivated by the observed variability in trace element isotopic and chemical compositions of primitive (SiO_2<52 wt %) basalts in southwest North America (SWNA) during the Cenozoic transition from subduction to extension. Specifically, we focus on processes that may explain the enigmatic observation that in some localities, basalts with low Ta/Th, consistent with parental melts in a subduction setting, have ε_{Nd} signatures consistent with continental lithospheric mantle (CLM). In locations with the oldest CLM (Proterozoic and Archean), Cenozoic basalts with low Ta/Th have ε_{Nd} well below zero. We model channelized magma transport through the CLM using simple 1D transport models to explore the extent to which diffusive and reactive mass exchange can modify Nd isotopic compositions via open system melt-wallrock interactions. For geologically reasonable channel spacings and volume fractions, we quantify the reactive assimilation rates required for incoming melt with a different ε_{Nd} than the wall-rock to undergo a substantial isotopic shift during ≈10 km channelized melt transport. In the presence of grain boundaries, enhanced diffusion between melt-rich channels and melt-poor surrounding rock contributes to isotopic equilibration, however this effect is not enough to explain observations; our models suggest a significant contribution from reactive assimilation of wall-rock. Additionally our models support the idea that the observed covariability in Ta/Th and ε_{Nd} in Cenozoic basalts cannot be attributed to transport alone and must also reflect the transition from subduction-related to extension-related parental melts in SWNA.

Plain Language Summary Over the past half century, the abundances and isotopic ratios of trace elements such as Nd in basalts have been widely used to infer aspects of the source region where mantle melting occurs. This assumes that when the mantle melts, trace element characteristics of source rocks are inherited by the generated melts and these are not further modified as melts ascend through the tectonic plate (lithosphere) to be erupted as basalt. We reassess this assumption inspired by enigmatic observations from southwest North America, where basalts that have undergone minimal processing (primitive basalts), show trace element characteristics of both the mantle lithosphere and of the asthenosphere. We use 1D transport models to show that melts moving in channels through the lithosphere may undergo significant trace element changes by interacting with the walls as they ascend, thereby explaining the observations with geologically reasonable scenarios.

1. Introduction

Over the past half century, the chemical and isotopic compositions of continental basalts have been widely used to infer aspects of the physical and chemical evolution of the continental lithospheric mantle (CLM) and underlying asthenosphere. An implicit assumption in this approach is that, after correction for crustal contamination, primitive basaltic rocks have incompatible trace element ratios and radiogenic isotopic compositions inherited from their mantle source rocks, the latter defined here as the portion of the upper mantle in which melting initiated. However, incompatible element and isotopic ratios of continental basalts need not reflect those values inherited from a single mantle source region. For example, mantle derived melts that ascend to the surface are likely aggregates of multiple parental melts that might themselves have different sources (e.g., Stracke, 2021). Even basaltic melts derived from a single source may be compositionally modified by open system interactions with their surroundings during extraction, migration and ascent through the mantle (Liu & Liang, 2017; Navon & Stolper, 1987; Stracke & Bourdon, 2009).

In this paper we are concerned with the latter possibility. A need to reevaluate the role of mantle wall rock interaction in influencing basalt trace element and isotopic compositions has arisen from a recent reassessment

Writing – original draft: Mousumi Roy, Kellen Malone
Writing – review & editing: Mousumi Roy, G. Lang Farmer

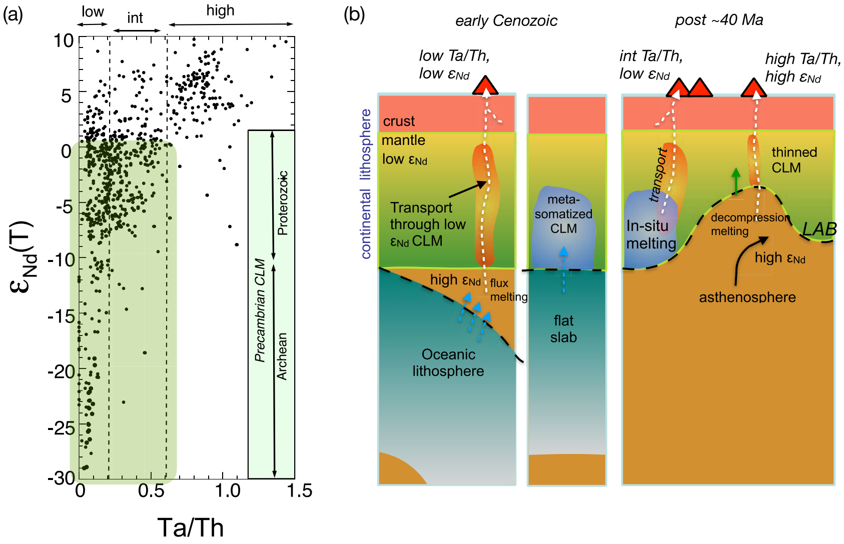

Figure 1. (a) ε_{Nd} versus Ta/Th in Cenozoic basalts with SiO_2 <52 wt% within SWNA (small black dots, N = 1,528, from Farmer et al. (2020)). Green boxes indicate range of ε_{Nd} observed in Cenozoic basalts ascending through older portions of the CLM, with ages as indicated. (b) Cartoon showing possible relationships between Cenozoic basalt Ta/Th and Nd isotopic compositions (ε_{Nd}) and CLM in regions underlain by Precambrian lithosphere in SWNA. *Left*: At end of the Cretaceous Era, thick low ε_{Nd} mantle lithosphere was underlain by the subducted oceanic Farallon plate. Hydrous fluids and volatiles drove flux melting in high ε_{Nd} asthenosphere, producing low Ta/Th in resulting basalts, which bear a low ε_{Nd} signature that may be a result of transport through thick CLM (as investigated here). *Middle*: Fluids from a low-angle subducted plate may have variably metasomatized the overlying CLM. *Right*: After removal of the Farallon slab, eruption of variable ε_{Nd} basalts may be due to in situ melting of metasomatized CLM (low ε_{Nd}, intermediate Ta/Th) and by upwelling and decompression melting of asthenosphere beneath thinned CLM (high ε_{Nd} and high Ta/Th). In each case, orange halos indicate zones where parental melts may interact extensively with CLM during ascent, as explored in our modeling.

of the extensive chemical and isotopic data available from Cretaceous and younger basaltic rocks in southwestern North America (SWNA). It has long been recognized in SWNA that many basalts are characterized by relatively non-radiogenic initial $^{143}Nd/^{144}Nd$ ratios, and $\varepsilon_{Nd}(T) < 0$, interpreted as evidence that their parental melts were sourced in low $\varepsilon_{Nd}(T)$ Precambrian CLM (Figure 1a; Fitton et al., 1988; Menzies et al., 1983) (In the following, we only refer to time-corrected $\varepsilon_{Nd}(T)$ values, and will drop the (T) for simplicity). But based on the entire compositional data set now available, it is now apparent that negative ε_{Nd} basaltic rocks can be subdivided into two distinct groups based on incompatible high field strength element ratios, specifically Ta/Th. One Ta/Th group corresponds to low ε_{Nd} basalts with Ta/Th <0.2, and with strongly correlated Ta and Th abundances ("low" Ta/Th group) that occur throughout SWNA (Farmer et al., 2020). Low Ta/Th values with strongly correlated Ta and Th abundances are characteristic of mafic to intermediate composition volcanic rocks in oceanic and continental arcs worldwide, and are generally interpreted as values inherited from melting of asthenospheric mantle wedge fluxed by volatiles derived from underlying oceanic lithosphere during active subduction (Figure 1b). The second low ε_{Nd} group has intermediate Ta/Th values, typically from 0.2 to 0.6, with decoupled Ta and Th abundances ("intermediate" Ta/Th group). Volcanic rocks with intermediate Ta/Th values are rare in oceanic settings, but common in SWNA where they typically occur after low Ta/Th group volcanism, although the absolute timing of the end of low Ta/Th and the onset of intermediate Ta/Th volcanism varies with geographic position. Intermediate Ta/Th volcanism in SWNA has been attributed to in situ melting of CLM metasomatized by fluids derived from oceanic lithosphere during low angle subduction that affected SWNA in the Late Cretaceous and Early Cenozoic (Figure 1b; Farmer, 2022; Farmer et al., 2020). The conundrum is that while low Ta/Th basaltic rocks are attributed to melting in high ε_{Nd} ($\varepsilon_{Nd} > 0$) asthenosphere and intermediate Ta/Th rocks represent in situ melting of low ε_{Nd} CLM, both sets of volcanic rocks have low ε_{Nd} values (Figure 1a). While a low ε_{Nd} value may arise from time-integrated effects of subduction-related modification of the asthenosphere (Chauvel et al., 2008; McCulloch & Gamble, 1991; Peate et al., 1997), Late Cretaceous basaltic rocks (with both low and intermediate Ta/Th values) in SWNA have ε_{Nd} values that correlate with the age of underlying Precambrian continental lithosphere: those underlain by Archean lithosphere have consistently lower ε_{Nd} than those underlain by lithosphere of Paleoproterozoic age (Figure 1a). This observation is still best explained by the derivation of Nd in these rocks from ancient CLM. One way to generate basalts that reflect both sub-lithospheric low Ta/Th magmas and a CLM-like Nd isotopic signature may be through interaction and partial-equilibration of high ε_{Nd} parental magmas during transport through thick, low ε_{Nd} CLM. Assessing this scenario is the goal of the current work. Motivated by the observations above, we test the possibility that lithospheric or sub-lithospheric parental melts may experience variable equilibration with thick, ancient CLM during transport (Figure 1b).

The effects of chemical and isotopic disequilibrium during melt generation and segregation in the mantle have been explored in numerical models for mid-ocean ridge and ocean island settings (e.g., Hauri, 1997; Iwamori, 1993; Kenyon, 1993). More recently, numerical models of disequilibrium reactive transport in porous flow highlight a richness of behavior that arises from diffusive exchange, particularly when it comes to interpreting trace element compositions (e.g., Oliveira et al., 2020, and refs within). This work builds upon these previous studies, particularly the approach of Hauri (1997), with the specific goal of considering the effects of chemical and isotopic disequilibrium during channelized transport of melts through the CLM. It is clear from detailed geochemical and petrologic characterization of exhumed CLM (e.g., in the Lherz and Ronda massifs) that isotopic, chemical, and thermal disequilibrium may exist across contacts between channelized melts and their surroundings (LeRoux et al., 2007, 2008; Soustelle et al., 2009). Here we use the term "channel" to denote a spatially limited melt-rich zone with a higher-than-ambient melt volume fraction (porosity), surrounded by material that is melt-poor (wall rock). Magma transport through the CLM is likely channelized at the macroscopic (10^{-1}–10^{1} m scale) (e.g., Katz et al., 2022, and refs within), probably in systems of ephemeral channels, and we consider the field relations in exhumed peridotite massifs to represent a primary mode of melt transport in the lower CLM (e.g., LeRoux et al., 2007, 2008; Soustelle et al., 2009). The models presented here are highly idealized in that they do not address the origin of channelization and parameterize averaged channel geometries and average motion of melt through the lower CLM. Our models also ignore thermochemical disequilibrium in major element compositions between the wallrock and melt-rich channels. Instead, the mass exchange in our models places limits on one process in particular, namely, trace element exchange by self-diffusion. They are, therefore, far from a complete representation of disequilibrium in channelized transport. Our purpose therefore is to use these calculations as a feasibility study to show that partial equilibration across channel walls may explain the conundrum in SWNA basalt trace element and Nd isotopic compositions described above. The open-system interactions we model concern Nd isotopic equilibration during transport and speculate on ways in which a CLM-like Nd isotopic signature may be imparted to melt within channels, while simultaneously preserving sublithospheric Ta/Th ratios.

We focus on diffusion and reaction (assimilation/precipitation) as two primary mass transfer mechanisms between channels and their surroundings, and explore the role of each. To investigate diffusive exchange between wall rock and channels, we consider a scenario where diffusion is strongly controlled by the configurational anisotropy that arises from the presence of grain boundaries in the wall material. Grain boundaries within the wallrock should be associated with both segregation of incompatible elements (Alard et al., 2022; Demouchy & Alard, 2021; Hiraga et al., 2004) and enhanced diffusive transport (Dohmen & Milke, 2010; Hiraga et al., 2007a, 2007b). We show that this leads to enhanced effective diffusivity, allowing diffusive exchange to reach further into wall rock (e.g., Jaseliūnaitė et al., 2022). Diffusive equilibration between an ascending, sublithosphere derived melt and surrounding CLM (when the two have a large initial isotopic contrast), however, cannot account for the Nd isotopic composition of basalts in SWNA. Instead, the observations require a role for mass transfer (via dissolution/precipitation) between wall rock and melt. Our simplified models ignore major-element chemical compositional variability within and between melt-rich and melt-poor parts of the system, building on Hauri (1997) (as described below). Our goal is to explore the regimes of behavior within a geologically relevant parameter space of channel spacing, volume fraction, fluid velocity, and likely Nd chemical and isotopic contrast across channel walls. Recognizing the limitations of an idealized model, we focus here on the degree of equilibration that may be established in 10 km of transport, a fraction of the CLM thickness. Our work establishes limits on the role of channel-wall diffusive exchange and reactive exchange, allowing us to assess the potential importance of isotopic shifts by mechanisms not included here, such as in-situ CLM melting, in generating low-silica basalts with CLM-like negative ε_{Nd}.

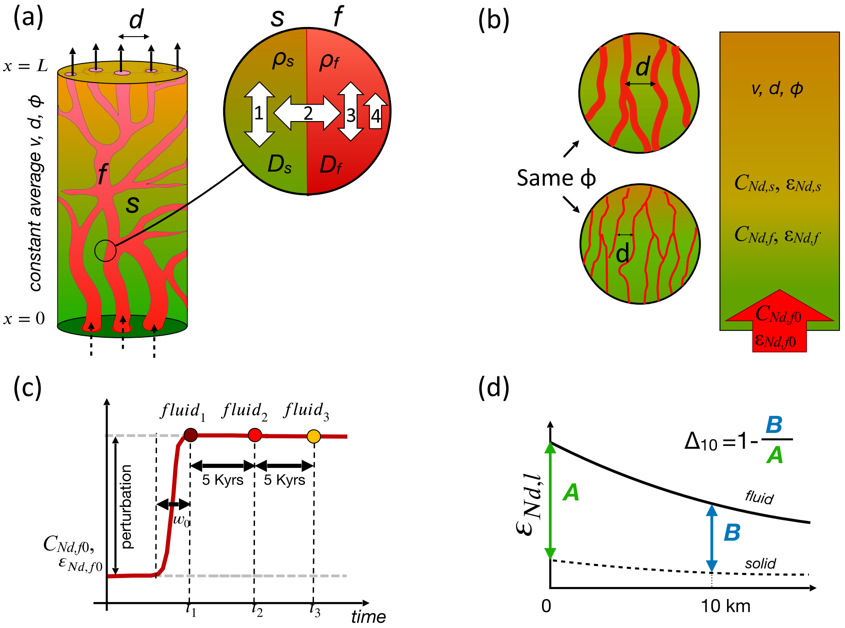

Figure 2. (a) Diagram of melt-rich channels ("fluid" $= f$, reddish) within a melt-poor region ("solid" $= s$, greenish). Melt-rich channels are spaced an average distance d apart with volume fraction ϕ; material in the channels has an average velocity v relative to the surrounding rock. The complex melt-transport system is idealized in a 1D model, valid over a length scale where d and ϕ maybe considered nearly constant, and which includes processes: (1) diffusion within the solid, (2) solid-fluid diffusion across the interface, (3) diffusion within the fluid, and (4) fluid advection. (b) Idealized 1D model with channel geometry parameterized by d, ϕ, and channel material velocity, v. As illustrated, changing d with a fixed ϕ is equivalent to changing the interphase contact area per unit volume, following Roy (2022). (c) Illustrates a step-like perturbation (with rise-time w_0) in ε_{Nd} and C_f imposed (only) within the incoming channel material at the inlet ($x = 0$). We define t_1 (maroon) as the first time the inlet value reaches the maximum perturbation (e.g., ε_{Nd} reaches +8), and $fluid_1$ as the fluid parcel that enters the domain at t_1. In Figure 4, we track the evolution of this parcel along with $fluid_2$ and $fluid_3$, entering at $t_2 = t_1 + 5$ Kyrs (red), and $t_3 = t_1 + 10$ Kyrs (yellow). (d) Definition of the degree of equilibration after 10 km of transport, Δ_{10}, illustrated in Figures 4 and 5a, based on the evolution of $fluid_1$ as it enters the domain.

2. Idealized Transport Model

We construct an idealized 1D schematic model where open system interactions in a real-world complex channel network (Figure 2a) are abstracted into a 1D domain containing melt-rich channels with moving material (here denoted as "fluid"; subscript f) and melt-poor stationary wall rock ("solid"; subscript s); Figure 2b. Our model is based on similar 1D approaches (Hauri, 1997; Roy, 2022, and references therein), however our work includes mass transfer (diffusive and reactive exchange) perpendicular to channel walls and diffusion along the transport direction within each of the fluid and solid domains. We use a set of modified advection-diffusion equations:

$$\frac{\partial C_f(x,t)}{\partial t} + v\frac{\partial C_f(x,t)}{\partial x} = -\frac{(1-\phi)\rho_s}{\phi\rho_f}\frac{1}{\tau_{ex}}\left(KC_f(x,t) - C_s(x,t)\right) + D_f\frac{\partial^2 C_f(x,t)}{\partial x^2} \tag{1}$$

$$\frac{\partial C_s(x,t)}{\partial t} = \frac{1}{\tau_{ex}}\left(KC_f(x,t) - C_s(x,t)\right) + D_s\frac{\partial^2 C_s(x,t)}{\partial x^2} \tag{2}$$

Here transport is assumed to be dominantly 1D (along $+\hat{x}$) with average relative velocity, v, between the material within the channels and outside (in a reference frame stationary with respect to the channel walls; Figure 2b). $C_f(x,t)$ and $C_s(x,t)$ represent the total concentration (mol/m^3) of the relevant isotopes of a trace element, in this case Nd, within and outside channels. The terms on the right hand sides of Equations 1 and 2 represent: (a) material exchange across channel walls and (b) diffusion within either the channel or the solid walls along the transport direction. The exchange term assumes that interaction across channel walls depends linearly on the degree of thermodynamic disequilibrium $\left(KC_f(x,t) - C_s(x,t)\right)$, where K is the mineral-melt partition coefficient,

Table 1
Material Properties and Nd Diffusion Constants Used in Calculations

Name	Symbol	Value or range	Source/comments
Nd concentration in solid	C_s	1 ppm	Byerly and Lassiter (2012)
Nd concentration in fluid	C_f	30 ppm	See Text S2 in Supporting Information S1
ε_{Nd} solid (CLM)	$\varepsilon_{Nd,s}$	−2	(−10)–(−2), D. J. DePaolo and Daley (2000)
ε_{Nd} fluid (Asthenosphere)	$\varepsilon_{Nd,f}$	+8	+7–+9, D. J. DePaolo and Daley (2000)
Bulk mineral-melt partition coefficient	K_{Nd}	0.0066	Salters and Longhi (1999), composition from Farmer et al. (2020)
In-channel melt velocity	$v_{channel}$	1 m/yr	1–10^2 m/yr, Katz et al. (2022)
{fluid, solid} Density	$\{\rho_f, \rho_s\}$	{2,800, 3,300} kg/m^3	Lesher and Spera (2015)
Channel flow coefficient	α	10	Bodinier et al. (1990) and Hauri (1997)
Separation of melt-rich channels	d	1–10^2 m	10^{-1}–10^3 m, LeRoux et al. (2008) and Braun and Kelemen (2002)
Volume fraction of melt-rich channels	ϕ	0.05–0.2	Liu and Liang (2017)
Nd diffusivity in fluid	D_f	10^{-11} m^2/s	Lesher (1994)
Nd diffusivity in crystals	D_x	10^{-19}–10^{-17} m^2/s	Tirone et al. (2005), VanOrman et al. (2002), and Ganguly et al. (1998)
Solid (grain boundary) diffusivity	D_{GB}	$10^4 D_x$	$D_{GB}/D_x = 10^{3-8}$, Hiraga et al. (2007a, 2007b) and Shewmon (1989)
Linear reaction rate	R	10^{-14}–10^{-13} m/s	Required to achieve $Da = [0,30]$ in Figure 5b
Effective solid diffusivity	D_s	$D_s = 10^{-17}$ m^2/s	Following Hiraga et al. (2007b) and Figure 3
Fluid perturbation rise time	w_0	1 Kyr	

Note. Citations in Supporting Information S1: D. DePaolo and Wasserburg (1976) and Walker et al. (2006).

following Hauri (1997) and Kenyon (1993) (see also Roy, 2022, for a similar treatment of thermal disequilibrium). The rate of mass exchange across channel walls depends on an exchange timescale, τ_{ex}, which depends upon the exchange mechanism (to be defined below). Other parameters include: the average channel spacing, d, and the average volume fraction of channels, ϕ, fluid and solid densities, ρ_f and ρ_s, and spatially uniform diffusion constants, D_f and D_s. Parameters and their values used here and elsewhere are listed in Table 1. We emphasize here that ϕ is the channel volume fraction, and not the fraction of melt in porous flow within the melt-poor channel walls. The range of values of ϕ considered, 5%–20%, are not well constrained but are comparable to those in exposed peridotite massifs (e.g., LeRoux et al., 2007; Soustelle et al., 2009). We assume that the effective diffusion coefficients (D_f, D_s) and bulk mineral-melt partition coefficient K are nearly indistinguishable for isotopes with high atomic number (Watkins et al., 2011, 2014, 2017), so these coefficients are assumed to be equal for all Nd isotopes. The bulk mineral-melt partition coefficient K used in this work is calculated from the partition coefficients for Nd in Salters and Longhi (1999) applied to the peridotite composition listed in Farmer et al. (2020).

To treat isotopic equilibration, we define $C(x,t) = C^{144}(x,t) + C^{143}(x,t)$, and the relative mol fraction of ^{144}Nd as $f \equiv C^{144}(x,t)/C(x,t)$. Substituting these into Equations 1 and 2 leads to the following expressions for the evolution of f in the fluid and solid, which are similar in form to (Johnson & DePaolo, 1994) (derivation of Equations S3 and S4 in Supporting Information S1):

$$\frac{\partial f_f}{\partial t} + v\frac{\partial f_f}{\partial x} = \frac{1}{C_f}\left(-\frac{(1-\phi)\rho_s}{\phi\rho_f}\frac{1}{\tau_{ex}}C_s\left(f_f - f_s\right) + 2D_f\frac{\partial f_f}{\partial x}\frac{\partial C_f}{\partial x} + D_f\frac{\partial^2 f_f}{\partial x^2}C_f\right) \tag{3}$$

$$\frac{\partial f_s}{\partial t} = \frac{1}{C_s}\left(\frac{1}{\tau_{ex}}KC_f\left(f_f - f_s\right) + 2D_s\frac{\partial f_s}{\partial x}\frac{\partial C_s}{\partial x} + D_s\frac{\partial^2 f_s}{\partial x^2}C_s\right) \tag{4}$$

This system of Equations 1–4 is applied to Nd in this study, but may be generally relevant to trace element exchange, where the concentration of the element is small. Here, we assume that any gradients in major element compositions and chemical activities will not affect diffusion of isotopes of Nd, a simplification further discussed below (but see Watkins et al., 2014). Additionally, by constraining our attention to ^{144}Nd and ^{143}Nd, we are assuming that gradients in the concentration of the other isotopes of Nd may be neglected assuming they will equally affect both isotopes in consideration (e.g., Du et al., 2022).

2.1. Effective Diffusivity in Channel Walls

The diffusivities employed here (Table 1) are based on the self-diffusivity of Nd (Lesher, 2010; Zhang, 2010), assuming that isotopic fractionation between ^{144}Nd and ^{143}Nd due to mass-dependent diffusivity is negligible (a power-law dependence on the mass ratio, e.g., Watkins et al., 2014). Although lattice (grain) diffusivity, D_x, for Nd is generally very low ($D_x = 10^{-19}$–10^{-17} m^2/s; Ganguly et al., 1998; VanOrman et al., 2002), it has long been recognized that the effective diffusivity, D_s, for peridotite (assumed channel wall rock) as a polycrystalline aggregate may be significantly larger. There are likely two mechanisms for this enhanced diffusion which governs exchange between channels and their surrounding walls: high diffusivity within grain boundaries and segregation of incompatible elements into inter-granular regions. In polycrystalline aggregates, the presence of grain boundaries may increase the effective diffusivity of Nd by $10^3 - 10^6$ above the lattice value (Hiraga et al., 2007a, 2007b), possibly up to a factor of 10^8 (Shewmon, 1989, although this is not well-constrained for mantle minerals; J. van Orman, personal communication). Additionally, segregation of incompatible elements into high-diffusivity grain boundaries can also play an important role in enhancing their mobility (Demouchy & Alard, 2021; Reddy et al., 2020).

We suggest that an additional (geometry-dependent) effect arises from the configurational anisotropy due to enhanced diffusion within grain boundaries. We demonstrate this in a 2D mesoscopic model, following Jaseliūnaitė et al. (2022), to illustrate the first-order effect of the presence of grain boundaries in an idealized model aggregate based on an actual peridotite thin-section (Figure 3). Hiraga et al. (2007b) suggests that the effective (bulk) diffusivity of the aggregate should be $D_s \approx D_x + s(3w/\delta)D_{GB}$, where D_x is the lattice (grain) diffusivity, D_{GB} is the diffusivity of the inter-grain regions, s is a segregation factor associated with enhanced storage of incompatible elements at grain boundaries, w is the grain boundary width, and δ is the average grain size. We assume that diffusivity in grain boundaries is enhanced by a factor $E = D_{GB}/D_x$ over the lattice value. If $E = 10^4$ (within the expected range $10^3 - 10^6$), then for aggregates with grain boundary width w on the order of 10^{-9} m and grain size d around 1 mm, Hiraga et al. (2007b) suggests that $s(3w/d) \approx 10^{-2}$ so that the effective diffusivity D_s should be a factor 10^2 larger than D_x. Using $E = 10^4$ for the model aggregate in Figure 3a, we find that the actual effective diffusivity D_s is around $\approx 5 \times 10^2$ larger than D_x, driven mainly by the effect of anisotropic diffusion in the presence of grain boundaries. The configurational anisotropy of high-diffusivity grain boundaries increases the wall-rock volume sampled by diffusive exchange (Figure 3c). A grain boundary enhancement of $E = 5 \times 10^4$ leads to an effective diffusivity of $D_s \approx 10^3 D_x$. In the following transport model, therefore, we take a conservative approach and consider a maximum value for the effective diffusivity in the channel walls of $D_s = 2 \times 10^{-17}$ m^2/s, about 200 times larger than the lattice diffusivity (Ganguly et al., 1998; VanOrman et al., 2002), but suggest that further work is needed to assess anisotropy-enhanced effective diffusivity.

2.2. Exchange Time Scale τ_{ex} and Dahmköhler Number

To solve the system of Equations 1–4, we non-dimensionalize and use a finite-difference approach (Text S3 in Supporting Information S1), parameterizing the model with a Damköhler number,

$$Da = \frac{(1-\phi)\rho_s}{\phi\rho_f}\frac{\tau_{ad}}{\tau_{ex}} \tag{5}$$

a dimensionless ratio of the time scale of melt advection $\tau_{ad} = L/v$ (L is the domain length) to the time scale of exchange between the fluid and solid τ_{ex}. The latter time scale depends upon the mechanism of mass transfer between material in the channels and the surrounding wall rock. For diffusion the relevant timescale is $\tau_d = d^2/(\alpha D_s)$ (Hauri, 1997), where α is a flow coefficient (=10 for channelized flow; e.g., Bodinier et al., 1990; Hauri, 1997). For reactive exchange, the timescale is instead $\tau_r = d/2R$, where R is a linear dissolution/precipitation rate (Hauri, 1997).

When both mechanisms are present, they each contribute an independent term proportional to the degree of disequilibrium on the right hand side of Equations 1–4, so that the Dahmköhler number Da depends on an

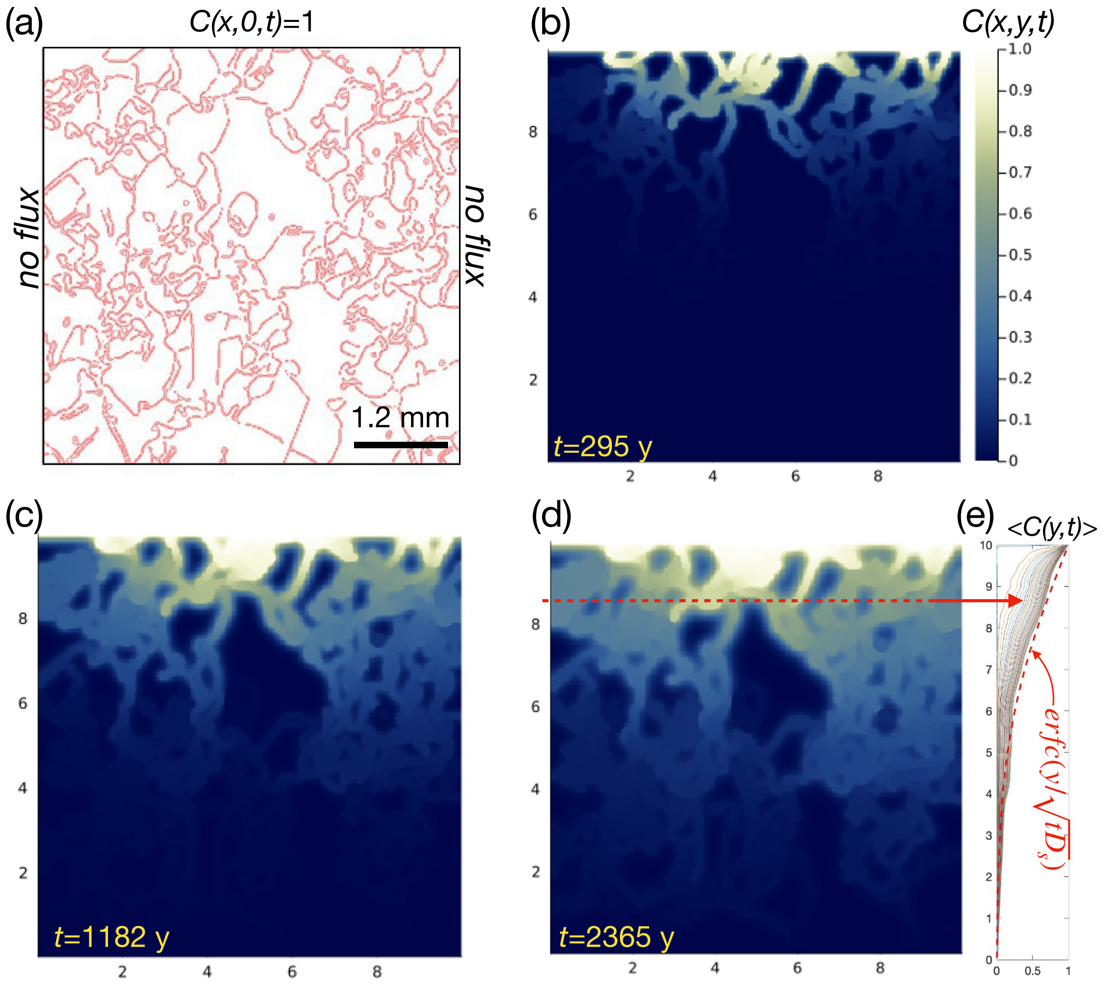

Figure 3. (a) Computational domain spanning ≈7–10 grains (256 × 256 elements) representing a random grain boundary configuration (red = grain boundaries, white = crystals), where crystals have a lattice diffusivity D_x and grain boundaries have a GB diffusivity $D_{GB} = 10^4 D_x$. The configuration of grains is digitized from a peridotite thin-section (from http://microckscopic.ro/). We solve the 2D diffusion equation for (dimensionless) concentration subject to boundary conditions shown on (a) and initial condition $C(x,y,t=0) = 0$ everywhere (see Text S4 in Supporting Information S1 for details). (b)–(d): Evolution of $C(x,y,t)$ for times indicated (these times are based on assuming the minimum D_x, 10^{-19} m^2/s), showing anisotropic diffusion into the domain. (e) Row-averaged concentration (direction of averaging indicated on (d)) through time with an effective diffusivity estimated by fitting $erfc\left(y/\sqrt{tD_s}\right)$ (red dashed line) to the concentration profile at time t.

effective exchange timescale, τ_{ex}, where $1/\tau_{ex} = 1/\tau_r + 1/\tau_d$, the harmonic mean of the timescale of both processes. The harmonic mean is appropriate when the processes are independent and the equilibration is simultaneously due to the lower-rate process (diffusion) and the higher-rate process (reaction): in effect, the two mechanisms are like resistors "in-parallel," so the effective timescale is not an arithmetic mean but rather a harmonic one. Through the timescale for diffusive exchange, τ_d, *Da* depends on the effective diffusivity in the wallrock, D_s, discussed above. Strictly, this depends on the diffusing species, and in this work we confine our attention to trace elements such as *Nd*. *Da* is a measure of the intensity of the fluid-solid mass exchange across channel walls within the domain relative to advection within the channels. For example, for a fixed volume fraction of channelized melt, ϕ, if the channel spacing, d, is decreased then the interphase contact area per unit volume increases (Figure 2b), decreasing τ_{ex} and increasing *Da*, leading to more vigorous exchange across channel walls (see also Figure S1 in Supporting Information S1).

2.3. Initial and Boundary Conditions

We study the transport Equations 1–4 subject to initial and boundary conditions as follows: initially the moving material in the channels is in equilibrium with the walls ($KC_{f0} = C_{s0}$), with no time variations (steady state). Then (at $t = 0$), the channelized material entering the domain at the inlet ($x = 0$) is subject to an imposed smoothed step-perturbation in chemical and isotopic composition (Figure 2c). The perturbation in isotopic and chemical composition of the fluid at the inlet ($x = 0$) begins at time $t = 0$, but is associated with a rise time w_0, the perturbation time scale. Therefore, for a given w_0, model behavior will be a strong function of the dimensionless time $\tau' = w_0/\tau_{ex}$. Following a transient response governed by two dimensionless numbers Da and τ', therefore, the system eventually returns to steady-state (no time-variations).

Characteristic values for initial and perturbed Nd chemical compositions are based on observations of mantle xenoliths and from Cenozoic basalt samples from SWNA (Text S2; Figure S3 in Supporting Information S1). Initially, $KC_f(x,0) = C_s(x,0)$ and $f_f(x,0) = f_s(x,0)$, where we assume $C_s(x,0) = C_{s0} = 1$ ppm and initial $\varepsilon_{Nd,f}(x,0) = \varepsilon_{Nd,s}(x,0) = -2$ (Table 1). We solve for the response of the system to a smoothed step-change imposed in both $C_f(0,t)$ and $\varepsilon_{Nd,f}(0,t)$ at the inlet ($x = 0$) at $t = 0$ (see Text S3 in Supporting Information S1 for functional form). The perturbation in $\varepsilon_{Nd,f}(0,t > 0)$ changes the fluid value from -2 to $+8$ and the perturbation in $C_f(0,t > 0)$ changes from $1/K$ to 30 ppm (Table 1; Text S2 in Supporting Information S1).

3. Results

To highlight the role of channel-wall mass exchange in determining the evolution of fluid composition, we present our results tracking the chemical and isotopic evolution of specific parcels of fluid, in a (Lagrangian) reference frame fixed to each parcel (cf. Farmer et al., 1997) (The subscript l indicates quantities in a given fluid parcel, e.g., C_{fl}, while quantities without l are in an Eulerian frame, e.g., C_f. See also Figure S2 in Supporting Information S1 for Eulerian profiles). Following the step-perturbation, we track 3 parcels of fluid, $fluid_1, fluid_2$, and $fluid_3$, entering the domain at various times t_1, t_2, and t_3 (Figure 2c). To quantify the degree of isotopic equilibration a parcel may undergo after, say, 10 km of transport, we define Δ_{10},

$$\Delta_{10} = 1 - \frac{(\varepsilon_{Nd,lf} - \varepsilon_{Nd,ls})_{x=10\ km}}{(\varepsilon_{Nd,lf} - \varepsilon_{Nd,ls})_{x=0\ km}} \tag{6}$$

where $(\varepsilon_{Nd,lf} - \varepsilon_{Nd,ls})$ is the (local) contrast between a fluid parcel and the solid wall adjacent to it (In Figures 4 and 5a, the reported Δ_{10} values are for the $fluid_1$ parcel in Figure 2c).

Three regimes of behavior are evident, governed by the dimensionless Da and τ' numbers, as follows (Figure 4): (I) small Da and τ', with minimal to no equilibration and exchange where chemical and isotopic contrasts between the fluid parcel and its surroundings are maintained over large transport distances, (II) intermediate Da and τ', with substantial exchange and partial equilibration over the model domain; and (III) large Da and τ', characterized by strong transverse mass exchange leading to (spatially varying) local equilibrium across channel walls.

In regime I, $\varepsilon_{Nd,l}$ values in both the fluid and the solid are barely modified after 10 km of transport, $\Delta_{10} \approx 0$ (no equilibration; Figure 4a) and the imposed disequilibrium between the fluid and the solid is preserved. By contrast in regime III, the exchange time scale is much smaller than the advection time scale so that the fluid and the solid are in nearly instantaneous local equilibrium: the solid composition (unphysically) tracks the perturbed fluid compositions as the parcel interacts with and passes the solid ($\Delta_{10} < 0$; Figure 4d). After $fluid_1$ has modified the solid domain, $fluid_2$ enters 5 Kyrs later and (unlike $fluid_1$) does not interact with unmodified solid upon entering the domain, but has to traverse several km before reaching the unmodified solid portion of the domain (e.g., Figure 4d). The same process happens for $fluid_3$, which enters 5 Kyrs after $fluid_2$, further increasing the distance needed to reach unmodified solid. Subsequent fluid parcels would continue needing more and more travel time to reach unmodified solid until the whole domain has been modified to the perturbation composition and any new fluid parcels entering the domain will have the same composition at the end of the domain as that at the inlet. The instantaneous equilibration in regime III (for high Da and τ' in Figure 4d) is likely to be unphysical for application to the real world. In this regime (particularly for large τ' where the perturbation timescale is long compared to exchange), the 1D models would allow infinite exchange, whereas in the real (3D) world equilibration fronts moving perpendicular to channel walls may meet and exhaust unmodified wallrock, limiting the amount of possible equilibration. Both regime I and regime III in the long-time limit are associated with fluid compositions that remain unchanged through the domain.

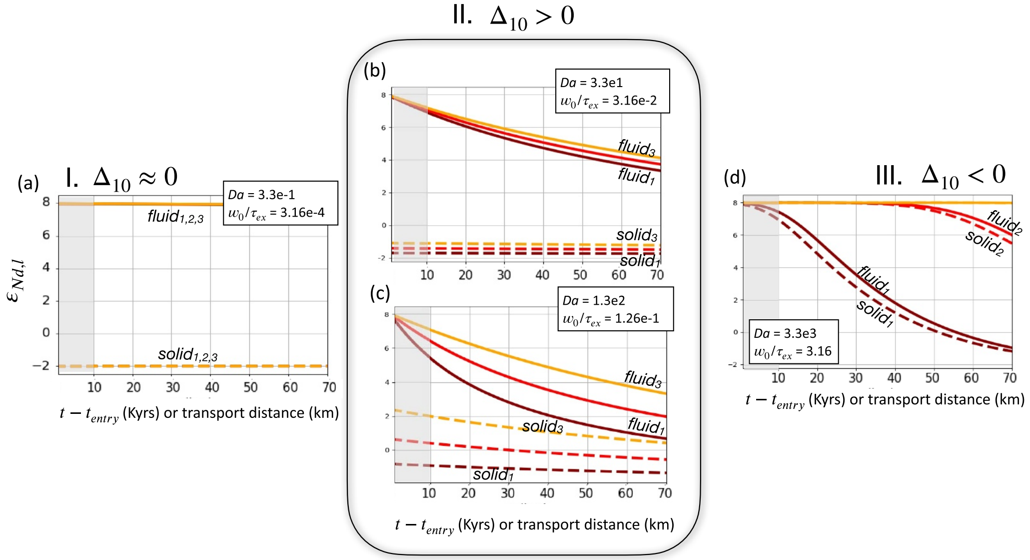

Figure 4. Tracking (Lagrangian) fluid isotopic evolution in response to a smoothed step-perturbation in both $C_{Nd,f}$ and $\varepsilon_{Nd,f}$, within fluid parcels that enter the domain with $\varepsilon_{Nd,l}$ of +8 (indicated as $fluid_1$, $fluid_2$, and $fluid_3$ as in Figure 2c). Profiles of $\varepsilon_{Nd,l,f}$ (solid lines), as well as the $\varepsilon_{Nd,L,s}$ adjacent to the parcel (dashed) are shown versus time since entry $(t - t_{entry})$. For relative fluid-solid velocity v = 1 m/yr, in a Lagrangian reference frame the time since entry in Kyrs is (relative distance traveled in km)/v; therefore, the numbers on the x−axis of the plots can also be read as transport distance, in km. Results are shown for varying Da and $\tau' = w_0/\tau_{ex}$, as indicated; other parameters are as in Table 1: $\phi = 0.1$, $D_f = 10^{-11}$ m^2/s, $D_s = 10^{-17}$ m^2/s, $w_0 = 1$ Kyr, $K = 0.0066$. In each case, the degree of equilibration after 10 km of transport (shaded gray region), Δ_{10} is indicated for $fluid_1$ (definition in text). Three regimes of behavior are evident: (I) $\Delta_{10} \approx 0$ (in (a), no equilibration), (II) $\Delta_{10} > 0$ (in (b) and (c), partial equilibration), (III) $\Delta_{10} < 0$ (in (d), local equilibrium). Corresponding profiles of $\varepsilon_{Nd,f}$ and $\varepsilon_{Nd,s}$ versus position in a domain-fixed reference frame (Eulerian) at different times are shown in Figure S2 of the Supporting Information S1.

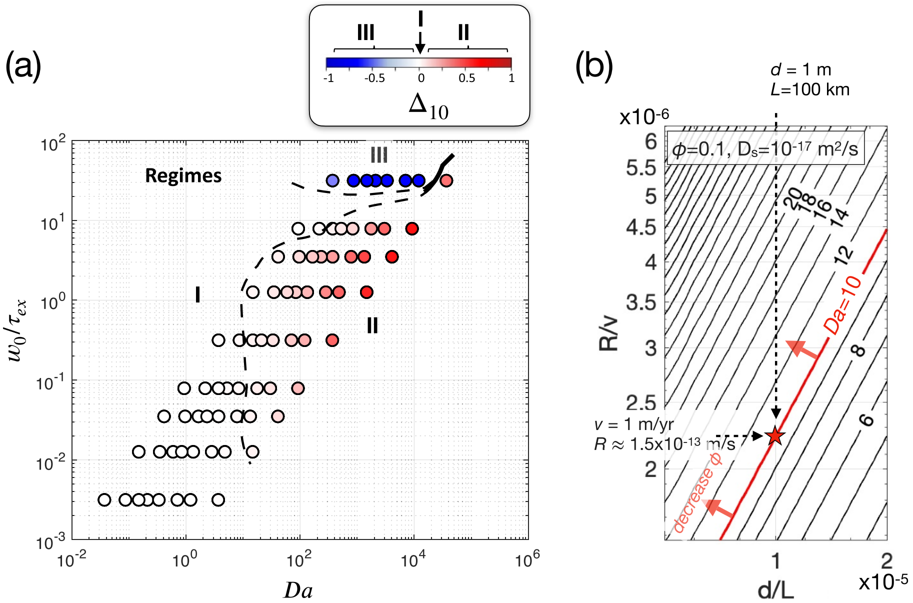

Figure 5. (a) Heat map of the degree of equilibration after 10 km of transport, Δ_{10}, as a function of dimensionless numbers Da and τ', assuming constant: v = 1 m/yr, $D_f = 10^{-11}$ m^2/s, $D_s = 10^{-17}$ m^2/s, w_0 = 1 Kyr, $K = 0.0066$. Regimes I, II, and III (dashed black lines) are determined as discussed in the text. (b) Contours of Da as a function of dimensionless channel spacing d/L and dimensionless reaction rate R/v. The red star on the $Da = 10$ contour corresponds to d = 1 m (for domain length L = 100 km), v = 1 m/yr and $R = 1.5 \times 10^{-13}$ m/s for a model with $\phi = 0.1$, $D_s = 10^{-17}$ m^2/s, w_0 = 1 Kyr, and $K = 0.0066$.

Regime II on the other hand is associated with partial equilibration during transport: the imposed disequilibrium between incoming fluid parcels and the surrounding solid persists, but the degree of disequilibrium decreases with transport ($0 < \Delta_{10} \leq 1$; Figures 4b and 4c). Like regime III, the solid is modified by each passing fluid parcel, so subsequent fluid entering the domain will not exit the domain with the same composition as fluid entering prior or after it. These regimes are summarized in a "phase diagram" of model behavior in the Da and τ' space (Figure 5a; for simplicity, we report Δ_{10} for $fluid_1$ in Figure 2c, which enters the inlet with $\varepsilon_{Nd,fl} = +8$). Generally, for partial Nd isotopic equilibration (regime II) between basaltic melts ($\varepsilon_{Nd} = +8$, ≈ 30 ppm Nd) and CLM (here $\varepsilon_{Nd} = -2$, 1 ppm Nd), we require $Da > 10$ (Figure 5a). As demonstrated in Figure 5b, if we use $D_s = 10^{-17}$ m^2/s as a reasonable solid diffusivity, $Da \geq 10$ may be achieved for a wide range of geologically reasonable parameters: for example, $Da = 10$ for $v = 1$ m/yr, $d = 1$ m, and a reaction rate of $R \approx 1.5 \times 10^{-13}$ m/s.

4. Discussion

The results above suggest that Nd isotopic equilibration during channelized transport maybe be categorized into three regimes of behavior as a function of the dimensionless Dahmköhler number Da and perturbation timescale τ' (Figure 5). This categorization also appears in other 1D melt transport models (Hauri, 1997; Kenyon, 1993) and in isotopic advection-reaction models for hydrothermal fluids moving through rock (Farmer et al., 1997), suggesting they are a generic feature of 1D fluid-solid advection-diffusion/reaction transport models. The applicability of these 1D results, and previous 1D approaches (Hauri, 1997; Kenyon, 1993), to magma transport within the CLM is limited as the approach is confined to a single transport direction with constant relative velocity v and constant geometry and material properties within the domain. The 3D effects of channel geometry (sinuosity, orientation, etc.) are combined into two scalars, d and ϕ, the channel spacing and volume fraction (cf. Roy, 2022). We mitigate this to some extent in this study, however, by confining our attention to short transport distances (≈ 10 km) and channel spacings $d \geq 1$ m, even though geologic observations support the idea of channelized flow at the sub-meter scale (e.g., Braun & Kelemen, 2002; LeRoux et al., 2008; Liang et al., 2010). We recognize that over $\approx$10 km of transport the ambient temperature in the CLM may vary by several tens of degrees (e.g., equilibrium thermal gradient of 5^{o}C/km) and one might expect thermally driven variations of material parameters (D_s, D_f, K; e.g., Van Orman et al., 1998). On the other hand, transient heating due to melt transport (e.g., Roy, 2022) may mitigate this effect. The lack of combined heat and mass-transfer across channel walls is a limitation of these 1D models, and beyond the scope of this study. Therefore, the models above are best regarded as representing the time-averaged effects of a stochastic transport process (e.g., an ensemble of ephemeral dikes or channels) within the CLM, when transport in a particular direction dominates over others. By considering $d \geq 1$ m, we adopt a conservative approach: our estimates of the degree of isotopic equilibration is likely a lower bound, as sub-meter spacings would likely lead to higher interphase contact area per unit volume and therefore more exchange across channel walls. Unlike melt distributed at the grain-scale (Hirth & Kohlstedt, 2003), the effect of the melt-rich channels on the overall rheology of the CLM is not well-understood, so it is difficult to quantify how the range of channel volume fraction ϕ here would affect the overall deformation of the lowermost CLM. Furthermore, processes such as reactive exchange via dissolution/precipitation may alter the channel geometry parameters (d and ϕ, assumed constant here). In this model, we ignore such feedbacks. With these caveats in mind, three robust results emerge for models with geologically reasonable channel spacings $d = 1$–100 m, channel volume fractions $\phi = 0.05$–0.2, and a conservative estimate for the effective Nd diffusivity in the channel walls $D_s = 10^{-17}$ m^2/s, as follows.

First, partial Nd isotopic equilibration during channelized transport within the CLM is achievable for $Da \geq 10$ for a broad range of perturbation timescales (regime II in Figures 4b and 5a). This situation is likely if the dimensionless linear reaction (assimilation) rate R/v is higher than 2×10^{-6} to 10^{-5}, which for a channel flow rate of v =1 m/yr leads to $R = 1.5 \times 10^{-13}$ m/s (Figure 5b). This conclusion is unchanged even if $D_s = D_x = 10^{-19}$ m^2/s is assumed, as the diffusive timescale is much longer than that for reaction so the exchange timescale, and therefore Da, is more strongly controlled by τ_r than τ_d. While the simulations above assume an in-channel advective velocity $v = 1$ m/yr, we do not specify the physical orientation of the transport direction $(+\hat{x})$. The results are therefore a first-order estimate to the degree of isotopic equilibration expected across channels of any orientation. Vertical melt ascent rates may however be up to 10^1 m/yr (e.g., Katz et al., 2022) and if transport direction is dominantly vertical with $v = 10$ m/yr instead of 1 m/yr (for $d = 1$ m, $\phi = 0.1$, $R = 1.5 \times 10^{-13}$ m/s), Da would be reduced from 10 to 1. In this case, reaching regime II would require a larger reaction rate,

$R = 10^{-12}$ m/s. To put these reaction rates in context, the kinetics of transient crystal dissolution and precipitation driven by chemical disequilibrium in a binary or ternary melt system (Liang, 2003) predict $R \approx 2 \times 10^{-11}$ m/s (for diffusion-in-solid limited dissolution) up to $R \approx 2 \times 10^{-8}$ m/s (for diffusion-in-melt limited dissolution). Linear reaction rates $R = 10^{-12}$–10^{-13} m/s needed to achieve $Da = 10$ for melt ascent rates $v = 1$–10 m/yr (e.g., for $d = 1$ m, and $\phi = 0.1$; Figure 5b), fall well below kinetically constrained dissolution/precipitation rates. Therefore, partial Nd equilibration in the presence of chemical and isotopic disequilibrium between infiltrating melts and their surrounding wallrock, a hallmark of regime II behavior in our models (Figures 4 and 5), is geologically feasible.

Second, if $Da \geq 10^2$, partial equilibration by open-system interactions over 10 km of transport is sufficient to achieve $\Delta_{10} \geq 0.5$ (Figure 5a). For a fluid parcel that enters the CLM with a maximum initial isotopic contrast of +10 epsilon units (e.g., for $fluid_1$ in our models $\varepsilon_{Nd,f0} = +8$ and $\varepsilon_{Nd,s0} = -2$), this is equivalent to an isotopic shift of 5 epsilon units. The transport distance needed to change the fluid $\varepsilon_{Nd,f}$ by a similar amount in subsequent fluid parcels, however, would be larger as the surrounding solid equilibrates toward the perturbed fluid value from earlier fluid parcels, thus decreasing the degree of disequilibrium between later-entering fluid parcels and the wallrock.

Third, returning to the observations of Cenozoic basalts in SWNA, this process would predict a temporal shift in ε_{Nd} in primitive basalts through time from low to high values, as corroborated by observations in specific localities such as the southern Rio Grande Rift (e.g., Figure 17 in Farmer et al. (2020)). Additionally, the CLM in SWNA has undergone significant thinning in Cenozoic time, which also drives the temporal shift in ε_{Nd}. For primitive basalts with subduction-related low Ta/Th but CLM-like negative ε_{Nd} (Figure 1a), our models suggest that one explanation may be a much lower Da for Ta and/or Th exchange (e.g., regime I, no equilibration) than for Nd (regime II, partial equilibration) during transport of these rocks. However, it is difficult to envision a scenario where trace element exchange is significantly slower for Ta and/or Th versus for Nd in the presence of a given channel network geometry, with wallrock-channel mass transfer via reactive assimilation and diffusive processes. An alternate explanation is that the infiltrating asthenospheric melts and lowermost CLM had similar, low Ta/Th values (<0.2) but the former had higher ε_{Nd} at the outset. Typical upper mantle has a Ta/Th $\widetilde{1}$ (Farmer et al., 2020) but there is evidence that subarc asthenosphere, even if initially involved in flux melting during active subduction, can be subsequently refertilized through interaction with low Ta/Th magmas as active subduction proceeds (Chin et al., 2014). This process imparts LREE enrichments and low Ta/Th values to the mantle. After cessation of subduction, and stabilization in continental lithosphere, this mantle develops increasingly negative ε_{Nd} values and isotopic disequilibrium with underlying convecting upper mantle, while retaining low Ta/Th values. If at least the base of the Precambrian mantle lithosphere in SWNA evolved In this fashion, then low Ta/Th asthenosphere-derived melts infiltrating the low Ta/Th base of the CLM during the Late Cretaceous and Cenozoic would have Nd isotopic compositions in disequilibrium across channel walls and therefore partially equilibrate, without substantially modifying the melt Ta/Th values.

The idea that channelized melt and wallrock experience different degrees of disequilibrium in the Nd isotopic and Ta/Th systems is supported by the observation that, in some parts of SWNA, the transition from low to high ε_{Nd} (and the correlated transition from low to high Ta/Th) occur progressively in time (Farmer, 2022; Farmer et al., 2020). In a subduction setting, where the upper plate CLM is infiltrated by high ε_{Nd} and low Ta/Th melts produced in the mantle wedge, our models would predict that regime III behavior is required for a progressive modification of the wallrock leading to a temporal transition from low to high ε_{Nd}. However, the end product of such progressive modification of wallrock would generate basalts with high ε_{Nd} and low Ta/Th, in contradiction with the observations (Figure 1a). This effectively rules out regime III behavior as an explanation for the correlated transition in Nd isotopes and in Ta/Th (Figure 1a). While the simultaneously low ε_{Nd} and low Ta/Th may be explained by partial Nd isotopic equilibration between a low Ta/Th (metasomatized) ancient CLM high Ta/Th (regime II behavior, as we have argued above), our models imply that protracted transport of melts derived from the mantle wedge through the CLM cannot explain the correlated increase in both ε_{Nd} and Ta/Th in SWNA alkali basalts. Instead, a different process must be invoked, namely, that the Ta/Th composition of infiltrating melts changes through time, from low to high values. A geologically reasonable scenario would be that, as SWNA underwent a transition from subduction to Neogene CLM thinning and extension, processes generating parental melts changed from flux-melting (low Ta/Th) to decompression melting (high Ta/Th; Figure 1b), with a concomitant shift in parental melt Ta/Th from low to high values.

5. Conclusions

We use idealized 1D transport models to provide a strong argument for reassessing the role of open-system interactions between channelized melt and its surrounding wallrock in driving trace element chemical and isotopic equilibration. Within the continental lithospheric mantle (CLM), where melt transport is likely to be channelized, our models constrain the relative importance of mass exchange across channel walls driven by both diffusion and reactive assimilation processes. We show that configurational anisotropy due to the presence of high-diffusivity grain boundaries may enhance the effective diffusivity of the wallrock, however, diffusion alone cannot drive partial equilibration between infiltrating melts and the CLM. Instead, for geologically reasonable parameters, we show that reactive assimilation is required for partial equilibration between channelized melts and the CLM. The models are used to explore the implications of observed Nd isotopic compositions and Ta/Th ratios in Cenozoic basalts from southwestern North America. Specifically, we show that partial equilibration of Nd isotopes during transport of parental melts through the CLM provides a mechanism to explain the observation of primitive basalts that have simultaneously low Ta/Th and low ε_{Nd}.

Data Availability Statement

Trace element geochemical data used in this study are identical to that in Farmer et al. (2020), with the criterion of wt. % $SiO_2 < 52$. These data are originally available from the NAVDAT/EarthChem database (http://portal.earthchem.org/ using the geographic and temporal criteria for Cenozoic basalts in southwestern North America). The models use Python and Julia; the codes are available at public repository, Roy (2024).

Acknowledgments

We thank thoughtful and detailed comments from two anonymous reviewers. We also thank A. Clark and T. Wickland for discussions and comments in the early stages of this study, and J. van Orman for discussions related to trace element diffusion in ultramafic rocks. This work was supported by NSF via Grants EAR-2052909 and EAR-2120812 to MR.

References

Alard, O., Halimulati, A., & Demouchy, S. (2022). Look between the grains. *Nature Geoscience*, *15*(11), 856–857. https://doi.org/10.1038/s41561-022-01065-3

Bodinier, J. L., Vasseur, G., Vernieres, J., Dupuy, C., & Fabries, J. (1990). Mechanisms of mantle metasomatism: Geochemical evidence from the Lherz orogenic peridotite. *Journal of Petrology*, *31*(3), 597–628. https://doi.org/10.1093/petrology/31.3.597

Braun, M., & Kelemen, P. (2002). Dunite distribution in the Oman ophiolite: Implications for melt flux through porous dunite conduits. *Geochemistry, Geophysics, Geosystems*, *3*(11), 1–21. https://doi.org/10.1029/2001gc000289

Byerly, B., & Lassiter, J. (2012). Evidence from mantle xenoliths for lithosphere removal beneath the central Rio Grande Rift. *Earth and Planetary Science Letters*, *355–356*, 82–93. https://doi.org/10.1016/j.epsl.2012.08.034

Chauvel, C., Lewin, E., Carpentier, M., Arndt, N. T., & Marini, J.-C. (2008). Role of recycled oceanic basalt and sediment in generating the Hf–Nd mantle array. *Nature Geoscience*, *1*(1), 64–67. https://doi.org/10.1038/ngeo.2007.51

Chin, E. J., Lee, C.-T. A., & Barnes, J. D. (2014). Thickening, refertilization, and the deep lithosphere filter in continental arcs: Constraints from major and trace elements and oxygen isotopes. *Earth and Planetary Science Letters*, *397*, 184–200. https://doi.org/10.1016/j.epsl.2014.04.022

Demouchy, S., & Alard, O. (2021). Hydrogen, trace, and ultra-trace element distribution in natural olivines. *Contributions to Mineralogy and Petrology*, *176*(4), 26. https://doi.org/10.1007/s00410-021-01778-5

DePaolo, D., & Wasserburg, G. (1976). Nd isotopic variations and petrogenetic models. *Geophysical Research Letters*, *3*(5), 249–252. https://doi.org/10.1029/gl003i005p00249

DePaolo, D. J., & Daley, E. E. (2000). Neodymium isotopes in basalts of the southwest basin and range and lithospheric thinning during continental extension. *Chemical Geology*, *169*(1–2), 157–185. https://doi.org/10.1016/s0009-2541(00)00261-8

Dohmen, R., & Milke, R. (2010). Diffusion in polycrystalline materials: Grain boundaries, mathematical models, and experimental data. *Reviews in Mineralogy and Geochemistry*, *72*(1), 921–970. https://doi.org/10.2138/rmg.2010.72.21

Du, J., Haley, B. A., Mix, A. C., Abbott, N., JamesMcManus, A., & Vance, D. (2022). Reactive-transport modeling of neodymium and its radiogenic isotope in deep-sea sediments: The roles of authigenesis, marine silicate weathering and reverse weathering. *Earth and Planetary Science Letters*, *596*, 117792. https://doi.org/10.1016/j.epsl.2022.117792

Farmer, G. L. (2022). Reassessing the role of continental lithospheric mantle in cenozoic magmatism, southwestern North America. In *Isotopic constraints on Earth system processes* (pp. 57–86).

Farmer, G. L., DePaolo, D. J., & Barnes, H. L. (1997). Sources of hydrothermal components: Heavy isotopes. *Geochemistry of Hydrothermal Ore Deposits*, *3*, 341–362.

Farmer, G. L., Fritz, D., & Glazner, A. F. (2020). Identifying metasomatized continental lithospheric mantle involvement in Cenozoic magmatism from Ta/Th values, southwestern North America. *Geochemistry, Geophysics, Geosystems*, *21*(5), e2019GC008499. https://doi.org/10.1029/2019GC008499

Fitton, J. G., James, D., Kempton, P., Ormerod, D., & Leeman, W. (1988). The role of lithospheric mantle in the generation of late Cenozoic basic magmas in the western United States. *Journal of Petrology*, (1), 331–349. https://doi.org/10.1093/petrology/special_volume.1.331

Ganguly, J., Tirone, M., & Hervig, R. L. (1998). Diffusion kinetics of samarium and neodymium in garnet, and a method for determining cooling rates of rocks. *Science*, *281*(5378), 805–807. https://doi.org/10.1126/science.281.5378.805

Hauri, E. (1997). Melt migration and mantle chromatography, 1: Simplified theory and conditions for chemical and isotopic decoupling. *Earth and Planetary Science Letters*, *153*(1–2), 1–19. https://doi.org/10.1016/s0012-821x(97)00157-x

Hiraga, T., Anderson, I. M., & Kohlstedt, D. L. (2004). Grain boundaries as reservoirs of incompatible elements in the Earth's mantle. *Nature*, *427*(6976), 699–703. https://doi.org/10.1038/nature02259

Hiraga, T., Hirschmann, M. M., & Kohlstedt, D. L. (2007a). Equilibrium interface segregation in the diopside–forsterite system I: Analytical techniques, thermodynamics, and segregation characteristics. *Geochimica et Cosmochimica Acta*, *71*(5), 1281–1289. https://doi.org/10.1016/j.gca.2006.11.020

Hiraga, T., Hirschmann, M. M., & Kohlstedt, D. L. (2007b). Equilibrium interface segregation in the diopside–forsterite system II: Applications of interface enrichment to mantle geochemistry. *Geochimica et Cosmochimica Acta*, *71*(5), 1281–1289. https://doi.org/10.1016/j.gca.2006.11.020

Hirth, G., & Kohlstedt, D. L. (2003). Rheology of the upper mantle and the mantle wedge: A view from the experimentalists. *Geophysical Monograph Series*, *138*, 83–105. https://doi.org/10.1029/138gm06

Iwamori, H. (1993). A model for disequilibrium mantle melting incorporating melt transport by porous and channel flows. *Nature*, *366*(6457), 734–737. https://doi.org/10.1038/366734a0

Jaseliūnaitė, J., Povilaitis, M., & Galdikas, A. (2022). Kinetic modeling of grain boundary diffusion: Typical, bi-modal, and semi-lamellar polycrystalline coating morphologies. *Coatings*, *12*(7), 992. https://doi.org/10.3390/coatings12070992

Johnson, T., & DePaolo, D. (1994). Interpretation of isotopic data in groundwater rock systems: Model development and application to Sr isotope data from Yucca Mountain. *Water Resources Research*, *30*(5), 1571–1587. https://doi.org/10.1029/94wr00157

Katz, R., Jones, D., Rudge, J., & Keller, T. (2022). Physics of melt extraction from the mantle: Speed and style. *Annual Review of Earth and Planetary Sciences*, *50*(1), 507–540. https://doi.org/10.1146/annurev-earth-032320-083704

Kenyon, P. (1993). Trace elements in migrating high-temperature fluids: Effects of diffusive exchange with the adjoining solid. *Journal of Geophysical Research*, *98*(B12), 22007–22020. https://doi.org/10.1029/93jb02265

LeRoux, V., Bodinier, J., Tommasi, A., Alard, O., Dautria, J., Vauchez, A., & Riches, A. (2007). The Lherz spinel lherzolite: Refertilized rather than pristine mantle. *Earth and Planetary Science Letters*, *259*(3–4), 599–612. https://doi.org/10.1016/j.epsl.2007.05.026

LeRoux, V., Bodinier, J.-L., Alard, O., O, S. Y., & Reilly, W. G. (2008). Isotopic decoupling during porous melt flow: A case-study in the Lherz peridotite. *Earth and Planetary Science Letters*, *279*(1–2), 76–85. https://doi.org/10.1016/j.epsl.2008.12.033

Lesher, C. E. (1994). Kinetics of Sr and Nd exchange in silicate liquids: Theory, experiments, and applications to uphill diffusion, isotopic equilibration, and irreversible mixing of magmas. *Journal of Geophysical Research*, *99*(B5), 9585–9604. https://doi.org/10.1029/94jb00469

Lesher, C. E. (2010). Self-diffusion in silicate melts: Theory, observations and applications to magmatic systems. *Reviews in Mineralogy and Geochemistry*, *72*(1), 269–309. https://doi.org/10.2138/rmg.2010.72.7

Lesher, C. E., & Spera, F. J. (2015). *Thermodynamic and transport properties of silicate melts and magma* (2nd ed.). Academic Press. (Chap. 5).

Liang, Y. (2003). Kinetics of crystal-melt reaction in partially molten silicates: 1. Grain scale processes. *Geochemistry, Geophysics, Geosystems*, *4*(5), 1045. https://doi.org/10.1029/2002gc000375

Liang, Y., Schiemenz, A., Hesse, M., Parmentier, E. M., & Hesthaven, J. S. (2010). High-porosity channels for melt migration in the mantle: Top is the dunite and bottom is the harzburgite and lherzolite. *Geophysical Research Letters*, *37*(15), L15306. https://doi.org/10.1029/2010gl044162

Liu, B., & Liang, Y. (2017). The prevalence of kilometer-scale heterogeneity in the source region of MORB upper mantle. *Science*, *3*(11). https://doi.org/10.1126/sciadv.1701872

McCulloch, M. T., & Gamble, J. (1991). Geochemical and geodynamical constraints on subduction zone magmatism. *Earth and Planetary Science Letters*, *102*(3–4), 358–374. https://doi.org/10.1016/0012-821x(91)90029-h

Menzies, M. A., Leeman, W. P., & Hawkesworth, C. J. (1983). Isotope geochemistry of Cenozoic volcanic rocks reveals mantle heterogeneity below western USA. *Nature*, *303*(5914), 205–209. https://doi.org/10.1038/303205a0

Navon, O., & Stolper, E. (1987). Geochemical consequences of melt percolation: The upper mantle as a chromatographic column. *The Journal of Geology*, *95*(3), 285–307. https://doi.org/10.1086/629131

Oliveira, B., Afonso, J. C., & Tilhac, R. (2020). A disequilibrium reactive transport model for mantle magmatism. *Journal of Petrology*, *61*(9), egaa067. https://doi.org/10.1093/petrology/egaa067

Peate, D. W., Pearce, J. A., Hawkesworth, C. J., Colley, H., Edwards, C. M., & Hirose, K. (1997). Geochemical variations in Vanuatu arc lavas: The role of subducted material and a variable mantle wedge composition. *Journal of Petrology*, *38*(10), 1331–1358. https://doi.org/10.1093/petrology/38.10.1331

Reddy, S. M., Saxey, D. W., Rickard, W. D., Fougerouse, D., Montalvo, S. D., Verberne, R., & Van Riessen, A. (2020). Atom probe tomography: Development and application to the geosciences. *Geostandards and Geoanalytical Research*, *44*(1), 5–50. https://doi.org/10.1111/ggr.12313

Roy, M. (2022). Assessing the role of thermal disequilibrium in the evolution of the lithosphere–asthenosphere boundary: An idealized model of heat exchange during channelized melt transport. *Solid Earth*, 13, 1415–1430. https://doi.org/10.5194/se-13-1415-2022

Roy, M. (2024). *mousumiroy-unm/endmelttransport: v1.0.1 (v1.0.1)*. Zenodo. https://doi.org/10.5281/zenodo.13732506

Salters, V. J., & Longhi, J. (1999). Trace element partitioning during the initial stages of melting beneath mid-ocean ridges. *Earth and Planetary Science Letters*, *166*(1–2), 15–30. https://doi.org/10.1016/s0012-821x(98)00271-4

Shewmon, P. (1989). *Diffusion in solids*. The Minerals, Metals, and Materials Society.

Soustelle, V., Tommasi, A., Bodinier, J. L., Garrido, C. J., & Vauchez, A. (2009). Deformation and reactive melttransport in the mantle lithosphere above a large-scale partial melting domain: The Ronda Peridotite Massif, southern Spain. *Journal of Petrology*, *50*(7), 1235–1266. https://doi.org/10.1093/petrology/egp032

Stracke, A. (2021). A process-oriented approach to mantle geochemistry. *Chemical Geology*, *579*, 120350. https://doi.org/10.1016/j.chemgeo.2021.120350

Stracke, A., & Bourdon, B. (2009). The importance of melt extraction for tracing mantle heterogeneity. *Geochimica et Cosmochimica Acta*, *73*(1), 218–238. https://doi.org/10.1016/j.gca.2008.10.015

Tirone, M., Ganguly, J., Dohmen, R., Langenhorst, F., Hervig, R., & Becker, H.-W. (2005). Rare Earth diffusion kinetics in garnet: Experimental studies and applications. *Geochimica et Cosmochimica Acta*, *69*(9), 2385–2398. https://doi.org/10.1016/j.gca.2004.09.025

Van Orman, J. A., Grove, T. L., & Shimizu, N. (1998). Uranium and thorium diffusion in diopside. *Earth and Planetary Science Letters*, *160*(3–4), 505–519. https://doi.org/10.1016/s0012-821x(98)00107-1

VanOrman, J. A., Grove, T. L., Shimizu, N., & Layne, G. D. (2002). Rare earth element diffusion in a natural pyrope crystal at 2.8 Gpa. *Contributions to Mineralogy and Petrology*, *142*(4), 416–424. https://doi.org/10.1007/s004100100304

Walker, J., Bowers, T., Black, R., Glazner, A., Farmer, G., & Carlson, R. (2006). A geochemical database for western North American volcanic and intrusive rocks (NAVDAT). *Special Paper—Geological Society of America*, *397*, 61–71.

Watkins, J. M., DePaolo, D. J., Ryerson, F. J., & Peterson, B. T. (2011). Influence of liquid structure on diffusive isotope separation in molten silicates and aqueous solutions. *Geochimica et Cosmochimica Acta*, *75*(11), 3103–3118. https://doi.org/10.1016/j.gca.2011.03.002

Watkins, J. M., DePaolo, D. J., & Watson, E. B. (2017). Kinetic fractionation of non-traditional stable isotopes by diffusion and crystal growth reactions. *Reviews in Mineralogy and Geochemistry*, *82*(1), 85–125. https://doi.org/10.2138/rmg.2017.82.4

Watkins, J. M., Liang, Y., Richter, F., Ryerson, F. J., & DePaolo, D. J. (2014). Diffusion of multi-isotopic chemical species in molten silicates. *Geochimica et Cosmochimica Acta*, *139*, 313–326. https://doi.org/10.1016/j.gca.2014.04.039

Zhang, Y. (2010). Diffusion in minerals and melts: Theoretical background. *Reviews in Mineralogy and Geochemistry*, *72*(1), 5–59. https://doi.org/10.2138/rmg.2010.72.2